# Rapid transform optimization strategy for decoherence-protected quantum register in diamond

Jiazhao Tian,[1,*] Haibin Liu,[2] Roberto Sailer,[3] Liantuan Xiao,[1,†] Fedor Jelezko,[3] and Ressa S. Said[3,‡]

[1]*School of Physics, Taiyuan University of Technology, Taiyuan 430000, People's Republic of China*

[2]*School of Physics, Hubei University, Wuhan 430062, People's Republic of China*

[3]*Institute for Quantum Optics and Center for Integrated Quantum Science and Technology, Ulm University, 89081 Ulm, Germany*

(Received 11 October 2023; accepted 10 January 2024; published 21 February 2024)

Decoherence-protected spins associated with nitrogen-vacancy color centers in diamond possess remarkably long coherence time, which makes them one of the most promising and robust quantum registers. The current demand is to explore practical rapid control strategies for preparing and manipulating such registers. Our work provides all-microwave control strategies optimized using multiple optimization methods to significantly reduce the processing time by 80% with a set of smooth near-zero-end-point control fields that are shown to be experimentally realizable. Furthermore, we optimize and analyze the robustness of these strategies under frequency and amplitude imperfections of the control fields, during which process we use only 16 samples to give a fair estimation of the robustness map with 2500 pixels. Overall, we provide a ready-to-implement recipe to facilitate high-performance information processing via a decoherence-protected quantum register for future quantum technology applications.

DOI: 10.1103/PhysRevA.109.022614

## I. INTRODUCTION

Nitrogen-vacancy color centers (NV centers) in diamond are an important candidate for future quantum computer registers as well as enhanced quantum sensors [1,2] because of their long coherence time. Utilizing the decoherence-free subspace (DFS) of the nuclear spin systems [3–5] can even prolong their coherence time and strengthen their advantages in future quantum technologies. A wide range of systems coded in DFS have been studied in areas of quantum computing and quantum sensing [6,7], including atoms [8], trapped ions [9,10], solid-state quantum dots [11], and so on [12–14]. Recently, a DFS strategy based on one $NV^-$ center and two nearby nuclear spins has been proposed, showing high resistance against static noises in the $\sigma_z$ direction [15]. In this strategy, the preparation and manipulation of the DFS are based on stimulated Raman adiabatic passage (STIRAP) driven by a microwave control field, avoiding the slow process of directly driving nuclear spins through the radio-frequency field. Nevertheless, the total transition time of the STIRAP strategy is still limited by the adiabatic condition. A method of superadiabatic STIRAP [16] can efficiently speed up the velocity by one order of magnitude, provided an auxiliary radio-frequency field is applied. However, the required strength of this radio field is in magnitude of megahertz, making it a challenge to faithfully achieve the field in experiment due to the nonlinear relationship between the Rabi frequency and the drive amplitude [17].

In this work we present the all-microwave control optimization strategies to construct and manipulate nuclear spins in the DFS of the NV-based nuclear system, decreasing the evolution time by one order of magnitude while maintaining the same fidelity. The control fields have smooth shapes and near-zero values at the beginning and ending points, making them feasible to be realized in experiments. As a recipe for optimization strategies in real experiments, we compare three common optimization methods, namely, the gradient-based gradient ascent pulse engineering (GRAPE) method [18], the multivariate function optimization chopped random basis (CRAB) method [19], and the phase-modulation (PM) method [20] in terms of the optimization result and speed for different evolution times. We show the simulated and experimental field shapes given by each method, confirming the experimental feasibility of these strategies. As the frequency and amplitude bias and the noise of the control field are inevitable in practice, we further make a fast estimation as well as optimization of the field robustness using the Bayesian estimation phase-modulated (BPM) method [21]. With this method only 16 samples are adequate to give the $50 \times 50$ pixel fidelity distribution map. In general, we supply a versatile, fast, and realistic toolbox of optimization methods to facilitate further implementations of the NV center as a quantum register and sensor.

The structure of the paper is as follows. In Sec. II we introduce the construction and manipulation strategy based on the decoherence-protected space of the NV-nuclear system. Section III represents optimization results of the GRAPE, CRAB, and PM methods in terms of fidelity, optimization speed, and field shape. Section IV investigates and analyzes the experimental feasibility of the optimization fields in terms of the real control shape given by control apparatuses (arbitrary wave generator and amplifier), as well as the robustness under frequency and amplitude bias, where we optimize this robustness using the BPM method. In Sec. V we provide a summary and discuss our results.

*tianjiazhao@tyut.edu.cn

†xiaoliantuan@tyut.edu.cn

‡ressa.said@uni-ulm.de

 

TABLE I. Parameter values in the total Hamiltonian [15].

| Parameter | Symbol | Value |
|---|---|---|
| zero-field splitting | $D$ | $2\pi \times 2.87$ GHz |
| gyromagnetic ratio of electron spin | $\gamma_e$ | $2\pi \times 2.8$ MHz/G |
| gyromagnetic ratio of nuclear spin | $\gamma_c$ | $2\pi \times 1.7$ kHz/G |
| dipolar coupling | $d_{12}$ | 4 kHz |
| isotropic hyperfine coupling | $A_{zz}^{(1)}$ | 12.45 MHz |
| isotropic hyperfine coupling | $A_{zz}^{(2)}$ | 2.28 MHz |

## II. DECOHERENCE-PROTECTED SPACE OF NUCLEAR SPINS

The system under consideration is a tripartite system comprising one $NV^-$ electron spin ($S = 1$) and two proximal $^{13}C$ nuclear spins ($I = 1/2$). The effect of near $^{14}N$ nuclear spins can be eliminated by polarization technology in experiment [22]. The total Hamiltonian of the system reads [15]

$$H = D\hat{S}_z^2 + \gamma_e \mathbf{B}\cdot\mathbf{S} + \mathbf{S}\cdot\sum_{i=1}^{2}\mathbb{A}^{(i)}\cdot\mathbf{I}^{(i)} + \gamma_c\mathbf{B}\cdot\sum_{i=1}^{2}\mathbf{I}^{(i)} + H_{nn}, \tag{1}$$

where $D\hat{S}_z^2$ is the zero-field term of the electron spin, $\gamma_e\mathbf{B}\cdot\mathbf{S}$ is the magnetic interaction of the electron spin, $\mathbf{S}\cdot\sum_{i=1}^{2}\mathbb{A}^{(i)}\cdot\mathbf{I}^{(i)}$ is the hyperfine coupling of the electron spin and the nuclear spins, $\gamma_c\mathbf{B}\cdot\sum_{i=1}^{2}\mathbf{I}^{(i)}$ is the magnetic interaction of the nuclear spin, and $H_{nn}$ is the dipole coupling between nuclear spins. The explicit forms of the hyperfine coupling tensor $\mathbb{A}^{(i)}$ for $i$th nuclear spin and $H_{nn}$, as well as the detail procedure to simplify the Hamiltonian, can be found in Appendix A. Hereafter, we use the simplified form

$$H = \begin{bmatrix} H^{m_s=0} & 0 \\ 0 & H^{m_s=1} \end{bmatrix}, \tag{2}$$

where $H^{m_s=0}$ and $H^{m_s=1}$ are the $4\times 4$ subspace Hamiltonians of two nuclear spins when the electron spin numbers are $m_s = 0$ and $m_s = 1$, respectively, with the explicit forms

$$H^{m_s=0} = \gamma_c B_z\left(\hat{I}_z^{(1)} + \hat{I}_z^{(2)}\right) + \gamma_c B_x\left(\hat{I}_x^{(1)} + \hat{I}_x^{(2)}\right) + \frac{d_{12}}{2}\left[\left(\hat{I}_+^{(1)}\hat{I}_-^{(2)} + \hat{I}_-^{(1)}\hat{I}_+^{(2)}\right) - 4\hat{I}_z^{(1)}\hat{I}_z^{(2)}\right] \tag{3}$$

and

$$H^{m_s=1} = (D + \gamma_e B_z)\mathbb{1} + A_{zz}^{(1)}\hat{I}_z^{(1)} + A_{zz}^{(2)}\hat{I}_z^{(2)}, \tag{4}$$

respectively, where $\mathbb{1}$ represents the $4\times 4$ identity matrix. The values of the parameters in Eqs. (3) and (4) are shown in Table I. Denoting the eigenstates and corresponding eigenvalues of $H$ by $|\psi_i\rangle$ and $E_i$, respectively ($i = 1, 2, \ldots, 8$), $H$ can be represented by $H = \sum_i E_i\hat{\sigma}_{ii}$, where $\hat{\sigma}_{ij} = |\psi_i\rangle\langle\psi_j|$. The explicit forms of $|\psi_i\rangle$ are shown in Fig. 1(b). Specifically, $|\psi_2\rangle$ has zero eigenvalue, $|\psi_3\rangle$ has near-zero eigenvalue (see caption of Fig. 1(b) and Appendix A for details), which makes both of these states robust against fluctuations of the magnetic field and possess long dephasing time. The states $|\psi_2\rangle$ and $|\psi_3\rangle$ therefore construct the decoherence-protected subspace.

To process logical qubit operations in the decoherence-protected subspace based on $|\psi_2\rangle$ and $|\psi_3\rangle$, one should first initialize the system into $|\psi_2\rangle$ or $|\psi_3\rangle$ and then carry out a flip-flop process between these two logic states. The initialization process follows the transitions $|0\uparrow\uparrow\rangle \to |\psi_1\rangle \to |\psi_2\rangle$, where the first step $|0\uparrow\uparrow\rangle \to |\psi_1\rangle$ can be completed by tuning the amplitude of the magnetic field in a timescale of 20 μs [15] (see Appendix B). The second step of the initialization

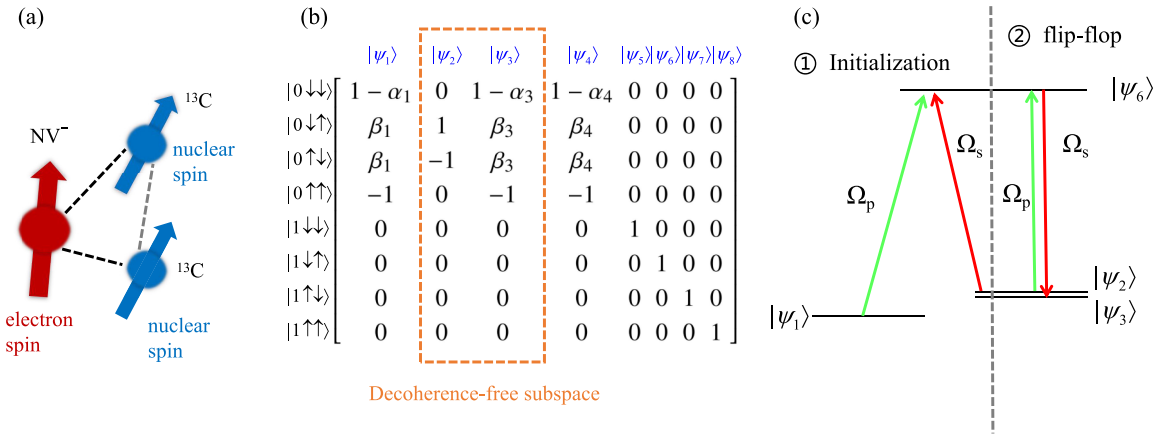


FIG. 1. (a) Triparticle system comprising one $NV^-$ electron spin ($S = 1$) and two proximal $^{13}C$ nuclear spins ($I = 1/2$). (b) Explicit formation of eigenstates (without normalization) of the Hamiltonian of the triparticle system shown in Eq. (2). For $j = 1, 3, 4$, $\alpha_j = \frac{(2d_{12}-2E_j)(-d_{12}-2E_j-2B_z\gamma_c)}{2B_x^2\gamma_c^2}$ and $\beta_j = \frac{-d_{12}-2E_j-2B_z\gamma_c}{2B_x\gamma_c}$, with $E_j$ the solution of the equation $-2d_{12}^3 - 4B_x^2 d_{12}\gamma_c^2 + 8B_z^2 d_{12}\gamma_c^2 - (3d_{12}^2 + 4B_x^2\gamma_c^2 + 4B_z^2\gamma_c^2)E_j + E_j^3 = 0$. The explicit values of $E_1$, $E_3$, and $E_4$ under different magnetic fields are shown in Appendix A. (c) Schematic diagram of the transition process $|\psi_1\rangle \to |\psi_2\rangle$ in the initialization step and $|\psi_2\rangle \to |\psi_3\rangle$ in the spin-flip step.

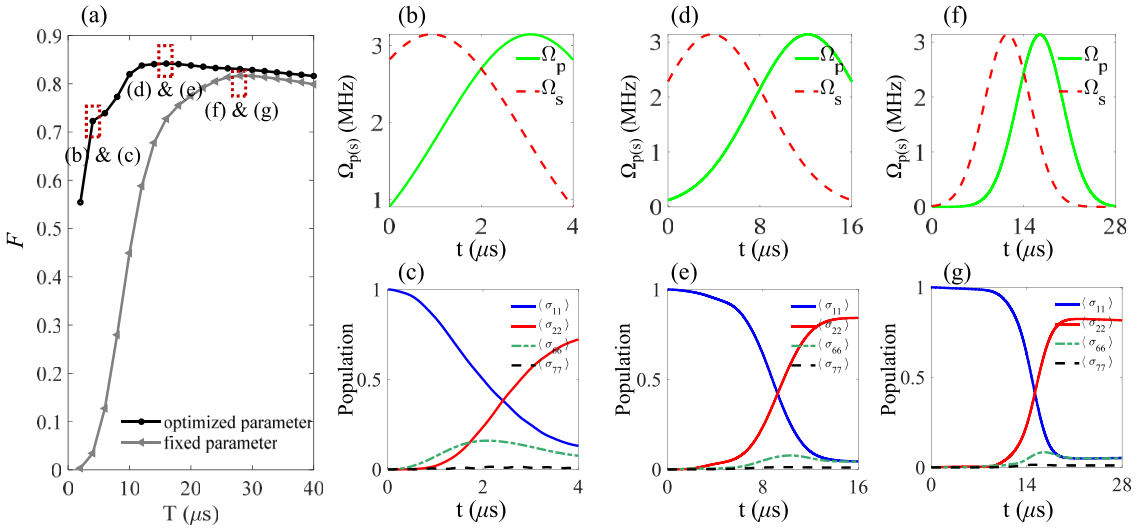


FIG. 2. (a) Transition efficiency of the process $|\psi_1\rangle \to |\psi_2\rangle$ given by STIRAP methods with a Gaussian-shaped control field following Eq. (10). The black line with dots shows the results with optimized parameters $\sigma$ and $t_d$. The gray line with triangles shows the results with fixed parameters $\sigma = T/8$ and $t_d = \sqrt{2}\sigma$. (b) and (c) Control field and population transition at $T = 4$ μs, with optimized parameters $\sigma = 1.95$ μs and $t_d = 2.15$ μs. (d) and (e) Control field and population transition at $T = 16$ μs, with optimized parameters $\sigma = 4.77$ μs and $t_d = 8.34$ μs. (f) and (g) Control field and population transition at $T = 28$ μs, with fixed parameters $\sigma = T/8 = 3.5$ μs and $t_d = \sqrt{2}\sigma = 4.95$ μs.

process, $|\psi_1\rangle \to |\psi_2\rangle$, and the flip-flop process $|\psi_2\rangle \leftrightarrow |\psi_3\rangle$ need to be driven by an external control field. Direct driving with a radio-frequency field is typically slow due to the low gyromagnetic ratios of the nuclear spin [23]. Although, in principle, increasing the intensity of the control field can speed up the driving process, in realistic experiments the dynamics of the nuclear spin oscillations becomes nonsinusoidal under a strong control field [17]. Indirect control with microwave fields using $m_s = 1$ states $|\psi_{5,6,7,8}\rangle$ as an intermediate circumvents this issue and achieves rapid transition [23].

Taking the transition from $|\psi_1\rangle$ to $|\psi_2\rangle$, for example, we write the driving Hamiltonian as

$$H_{\rm d} = [\sqrt{2}\Omega_p \cos(\omega_p t) + \sqrt{2}\Omega_s \cos(\omega_s t)]\hat{S}_x, \tag{5}$$

where $\Omega_{p\,(s)}$ and $\omega_{p\,(s)}$ are the amplitudes and the frequencies of two MW fields with $\omega_p = E_6 - E_1$, $\omega_s = E_6 - E_2$, and $\hat{S}_x = (|1\rangle\langle 0| + |0\rangle\langle 1|)/\sqrt{2}$. For brevity, we use the interaction Hamiltonian with respect to

$$H_0 = E_1\sigma_{11} + E_2\sigma_{22} + E_6\sum_{i=5}^{8}\sigma_{ii}. \tag{6}$$

After neglecting rapid oscillation terms, we obtain the interaction Hamiltonian with the rotating-wave approximation

$$H^I_{\rm RWA} = \frac{\Omega_p(t)}{2}(\chi_{51}\hat{\sigma}_{51} + \chi_{61}\hat{\sigma}_{61} + \chi_{71}\hat{\sigma}_{71} + \chi_{81}\hat{\sigma}_{81} + \text{H.c.}) + \frac{\Omega_s(t)}{2}(\chi_{62}\hat{\sigma}_{62} + \chi_{72}\hat{\sigma}_{72} + \text{H.c.}) + (H - H_0), \tag{7}$$

with $\chi_{ij} = \langle\psi_i|\hat{V}|\psi_j\rangle$ and $\hat{V} = \sqrt{2}\hat{S}_x$. A detailed derivation can be found in Appendix C. Considering transverse relaxations, evolution of the triparticle system can be described by the Lindblad master equation

$$\frac{{\rm d}\rho(t)}{{\rm d}t} = -i[H^I, \rho] + \mathcal{L}_S + \mathcal{L}_I, \tag{8}$$

where $\mathcal{L}_S = (1/T_2^*)(2\hat{S}_z\rho\hat{S}_z - \hat{S}_z^2\rho - \rho\hat{S}_z^2)$ is the dissipation term of the electron spin and $\mathcal{L}_I = \sum_{i=1}^{2}(1/T_{2n_i}^*)(2\hat{I}_z^{(i)}\rho\hat{I}_z^{(i)} - \hat{I}_z^{(i)^2}\rho - \rho\hat{I}_z^{(i)^2})$ is the dissipation term of the nuclear spins. Here the coherence times are taken as $T_2^* = 7$ μs, $T_{2n_1}^* = 500$ μs, and $T_{2n_2}^* = 700$ μs [15]. The transition effectiveness for a certain evolution time $T$ can be measured by the fidelity between the final density matrix $\rho(T)$ and the target density matrix $|\psi_2\rangle\langle\psi_2|$, represented by [18]

$$F = {\rm Tr}[\langle\psi_2|\rho(T)|\psi_2\rangle]. \tag{9}$$

One conventional strategy to complete the state transition with high fidelity is the STIRAP, where the amplitudes of control fields take the Gaussian shape

$$\Omega_p(t) = \Omega_0 \exp[-(t - t_d/2)^2/2\sigma^2],$$
$$\Omega_s(t) = \Omega_0 \exp[-(t + t_d/2)^2/2\sigma^2]. \tag{10}$$

As shown in Fig. 2(a), this adiabatic transition (with $\sigma = T/8$ and $t_d = \sqrt{2}\sigma$) needs the evolution time $T \geqslant 24$ μs to obtain fidelities of $F \geqslant 0.8$. When $T$ decreases to 4 μs, the fidelity drops to $F = 0.034$. We optimize the values of the parameters $t_d$ and $\sigma$ by a direct search method to obtain the highest fidelity for different evolution times, which increase the fidelity to $F = 0.842$ at $T = 16$ μs. However, the fidelity at $T = 4$ μs is still as low as $F = 0.723$. In addition, as shown in Figs. 2(b) and 2(d), the optimized control fields have beginning or ending values around 2–3 MHz. In practical experiments, such fields with nonzero end points could be distorted more severely due to the bandwidth limitation of the amplifier, thus decreasing the final fidelity. Different strategies

are essential to improve the results with higher fidelity and more practical field shape.

## III. OPTIMIZATION

In what follows we show how various optimization methods improve the low transition efficiency of STIRAP when the evolution time is reduced to several microseconds. We consider three widely used methods: the GRAPE [18], CRAB [19], and PM methods [20]. The GRAPE method is an exploitative method, in the sense that it updates each pulse section along the gradient ascending direction, and the value of its objective function will converge to a local optimum. In contrast, the CRAB and PM methods are explorative based on the global search method, where the expansion coefficients of the control fields are taken as the optimization parameters. Both methods use truncated expansion, while the CRAB method features randomization of the frequencies and the PM method features phase-modulation formation to improve the optimization efficiency.

Considering the transition process from $|\psi_1\rangle$ to $|\psi_2\rangle$ and taking the fidelity $F$ in Eq. (9) as the objective function, all three methods give the optimal shapes of control fields $\Omega_p(t)$ and $\Omega_s(t)$ that maximize $F$ under the constraint $\Omega_{p\,(s)}(t) \leqslant \Omega_{\max}$, where we set the maximum field amplitude as $\Omega_{\max} = \pi$ MHz. We use a boundary function [24] $\lambda(t) = h^p/[h^p - (t-h)^p]$, with $h = T/2$ and $p = 30$, to obtain a near-zero value of starting and ending points, which makes the control fields more practical in experiments. The stopping criterion is set as the termination tolerance of the function value being less than $10^{-4}$.

For the GRAPE method, $\Omega_p$ and $\Omega_s$ are constructed by $N$ pulses respectively with equal width $\Delta T = T/N$, and the optimization parameters are the amplitudes of these $2N$ pulses represented by $u_j^p$ and $u_j^s$, respectively, with $j = 1, 2, \ldots, N$. Considering the local property of the GRAPE method, we use two types of initial values to explore the optimums in a larger range. One is denoted by GRAPE($1/\lambda$), with initial field $\Omega_{p\,(s)}(t) = \Omega_0/\lambda(t)$, where $\Omega_0$ is uniformly distributed random number in the range $[0.5\pi, 0.9\pi]$ MHz. The other is denoted by GRAPE(G), with the Gaussian-shaped initial field in Eq. (10) with $\sigma$ randomly taken from [0.3, 3] μs, $t_d = \sqrt{2}\sigma$, and $\Omega_0 = 0.9\pi$ MHz. In each interaction of the GRAPE process, these pulses are updated successively according to the format [18]

$$u_j^{p\,(s)} = u_j^{p\,(s)} + \epsilon \frac{\partial F}{\partial u_j^{p\,(s)}}, \tag{11}$$

where $\epsilon$ is the interaction step length, the value of which should be set properly to guarantee the convergence of $F$. Meanwhile, the explicit forms of control fields in the CRAB method are

$$\Omega_p = \frac{1}{\lambda(t)} \sum_{n=1}^{N_c} [A_n \sin(\omega_n t) + B_n \cos(\omega_n t)], \tag{12}$$

$$\Omega_s = \frac{1}{\lambda(t)} \sum_{n=1}^{N_c} [C_n \sin(\omega_n t) + D_n \cos(\omega_n t)], \tag{13}$$

where $\omega_n = 2\pi n(1 + r_k)/T$ ($r_k \in [-0.5, 0.5]$) represents random numbers with flat distribution [19]. For the PM method, the explicit forms of the control fields are

$$\Omega_p = \frac{1}{\lambda(t)} \sum_{n=1}^{N_c} a_n \cos\left(\frac{b_n}{v_n} \cos(v_n t)\right), \tag{14}$$

$$\Omega_s = \frac{1}{\lambda(t)} \sum_{n=1}^{N_c} a_n \cos\left(\frac{b_n}{v_n} \sin(v_n t)\right). \tag{15}$$

The optimization parameters of the CRAB and PM methods are the $N_c \times 4$ matrix $[\boldsymbol{A}, \boldsymbol{B}, \boldsymbol{C}, \boldsymbol{D}]$ and the $N_c \times 3$ matrix $[\boldsymbol{a}, \boldsymbol{b}, \boldsymbol{v}]$, respectively, where $\boldsymbol{A} = [A_1, A_2, \ldots, A_n]'$; other vectors have similar forms. Here we take $N_c = 3$, which corresponds to fewer harmonics and hence is more friendly to control apparatuses.

Figure 3(a) shows the optimization fidelity given by the GRAPE, CRAB, and PM methods for different evolution times. At $T = 4$ μs, the GRAPE method with both kinds of initial values gives $F \approx 0.82$ [0.82 for GRAPE(G) and 0.817 for GRAPE($1/\lambda$) explicitly] and the PM method gives $F = 0.8$. The CRAB method only reaches $F = 0.683$. The highest fidelity 0.848 appears at $T = 11$ μs. Comparing the results of different methods, we see that the GRAPE(G) method shows a stable performance at different time conditions, while the GRAPE($1/\lambda$) method performs poorly for longer evolution times. The PM method is more likely to give the highest fidelity when $T \geqslant 7$ μs but can also give bad results at a few time points; this instability indicates a lack of total trial numbers. The CRAB method falls behind in both aspects of highest fidelity and stability. Overall, the fidelity exceeds 0.8 when $T \geqslant 4$ μs, indicating that 4 μs is the shortest time required to efficiently complete the transformation. A comparison of the optimization speeds of two direct search methods (PM and CRAB) is shown in the inset of Fig. 3(a), evaluated by the average calling number of objective functions. On a timescale of $T < 10$ μs, the CRAB method shows a speed advantage, and when $T > 10$ μs, the CRAB and PM methods show similar behaviors. Explicit population transitions at $T = 4$ μs are shown in Figs. 3(b)–3(d).

## IV. EXPERIMENTAL FEASIBILITY

The main concern regarding the experimental feasibility is whether the optimized field can be accurately realized in the experiments. To test and demonstrate such experimental feasibility, we generate the control fields using an arbitrary wave generator (Tektronix AWG-70002A, connected with the software Qudi) and measure the output electronic signal by an oscilloscope (LeCroy-WaveAce 234). The bandwidth of our arbitrary wave generator (AWG) is 14 GHz and the amplitude resolution is 10 bits. We denote the optimized simulation pulse sequences by $u_{\text{sim}}$, which comprising $N = T/\Delta T$ flat pulses $u_{\text{sim}}(i)$ ($i = 1, 2, \ldots, N$) with a pulse length of $\Delta T$. Similarly, the measured amplitudes of the pulse sequences are denoted by $u_{\text{real}}$, which comprises $u_{\text{real}}(i)$ ($i = 1, 2, \ldots, N$). To compare the shapes of the simulation and real pulses, we translate the values of the measured signal to make sure they begin from zero and scale them by a factor of $d_{\text{sim}}/d_{\text{real}}$,

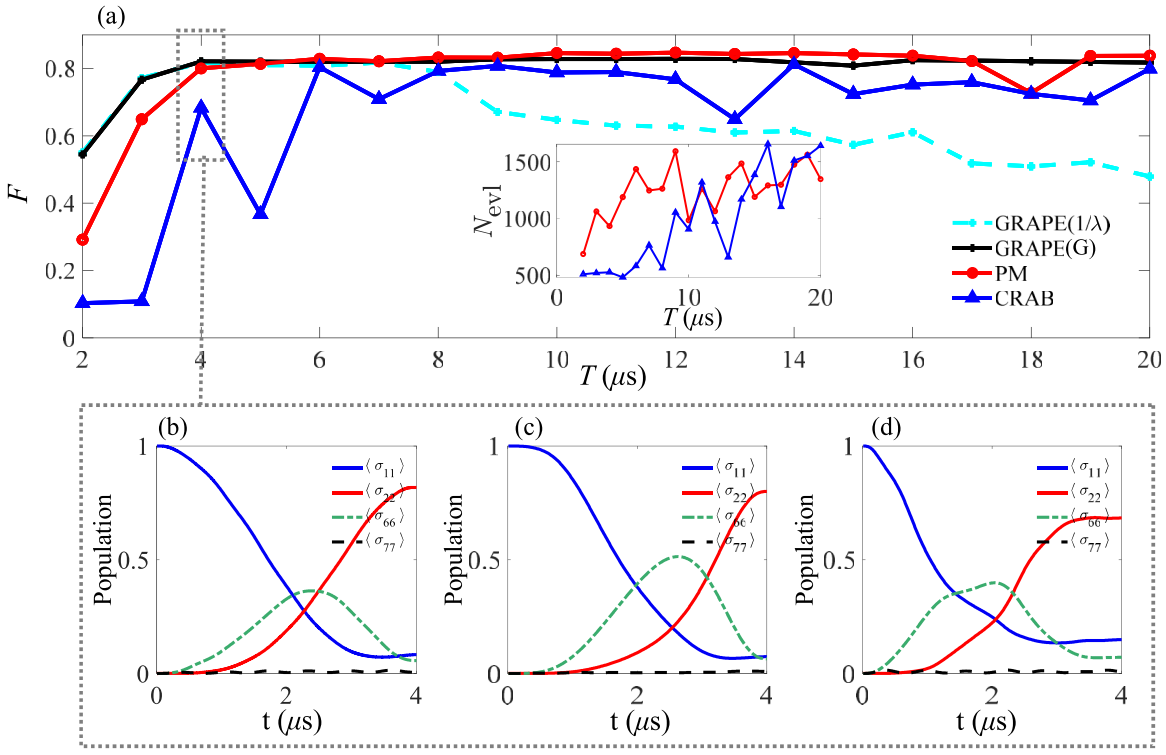


FIG. 3. (a) Optimization fidelity with different optimization methods for different evolution times. The inset shows the average number of functions evaluated by the PM and CRAB methods. Also shown is the population transition at $T = 4$ μs, given by the (b) GRAPE(G), (c) PM, and (d) CRAB methods.

where $d_{\text{sim}} = \max|u_{\text{sim}}| - |u_{\text{sim}}(1)|$ is the difference between the maximal amplitude and the amplitude of the beginning pulse of the simulation control field and $d_{\text{real}} = \max|u_{\text{real}}| - |u_{\text{real}}(1)|$ is the difference between the maximal amplitude and the amplitude of the beginning pulse of the output pulse sequence. The comparison results are shown in Fig. 4, where the real pulse shapes are broadly consistent with the simulation pulse shapes, which implies the optimization methods are indeed feasible in practice. Details of the experiment and the true values for conversion between the voltage signal and Rabi frequency are given in Appendix E.

In practical experiments, besides the limitation of the available bandwidth of the AWG and amplifier, another inevitable disturbance of the transition efficiency is the noise originating from ambient nuclear spins and external bias fields, which can be represented as the fluctuation of the amplitude as well as the detuning of the control field. Using the optimal PM control field shown in Figs. 4(b) and 4(e), we calculate the fidelity for different values of detuning and amplitude bias of the control field; the results are shown in Fig. 5(a). Such a distribution map contains $50 \times 50$ pixels, requiring 2500 calculation times of the evolution function. Using the

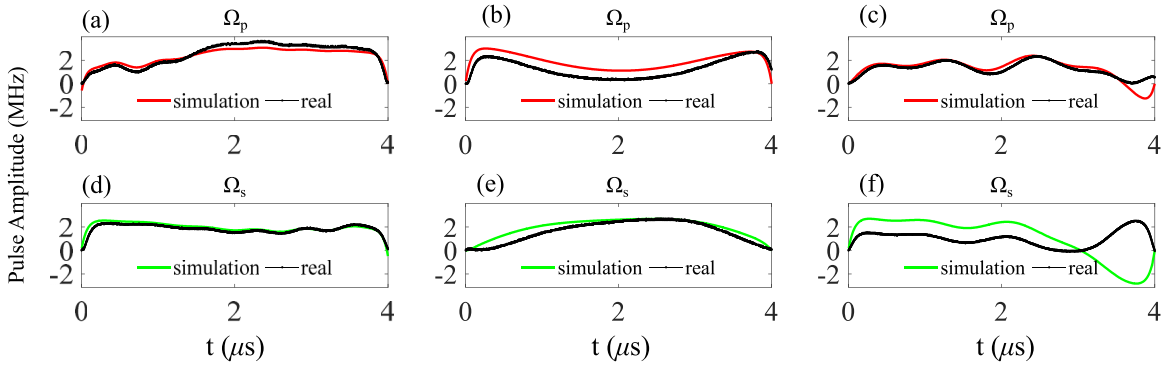


FIG. 4. Comparison of the simulation pulse and the real pulse generated by the AWG (Tektronix AWG-70002A, connected with the software Qudi) and measured by the oscilloscope (LECROY-WAVEACE 234) after a rf amplifier (Model No. 60S1G4AM3, AR Germany with frequency bandwidth 0.7–4.2 GHz and gain power of 60 W) for the same gain level. The simulation pulses are given by different optimization methods: (a) and (d) GRAPE, (b) and (e) PM, and (c) and (f) CRAB. The amplitudes of the measured values of the real pulses are scaled to make a direct comparison visible (see the text for details).

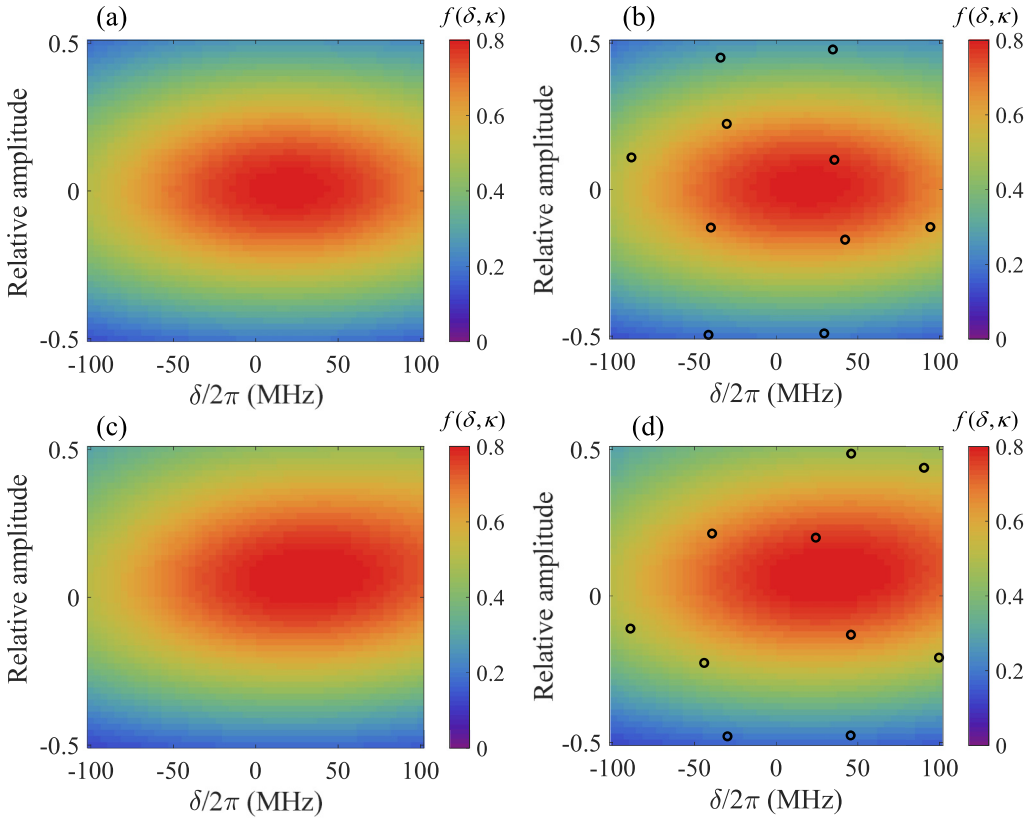


FIG. 5. (a) Simulated fidelity of the transition process from $|\psi_1\rangle$ to $|\psi_2\rangle$ for different values of detuning and amplitude bias of the control field. The total evolution time is $T = 4$ μs and the control field is given by the PM method, shown in Figs. 4(b) and 4(e). (b) Estimation values of the fidelity using the Bayesian-based estimation method. The black circles represent the locations of the samples. We used 16 randomly chosen sample points; only those with locations within the range ($\delta/2\pi \in [-100, 100]$ MHz, $\kappa \in [-0.5, 0.5]$) are shown. (c) Simulated fidelity of the control field optimized by the BPM method. (d) Estimation values of the fidelity using the Bayesian-based estimation method with the optimized field given by the BPM method. The black circles represent the location of samples. We used 16 randomly chosen sample points; only those with locations within the range ($\delta/2\pi \in [-100, 100]$ MHz, $\kappa \in [-0.5, 0.5]$) are shown.

Bayesian-estimation method [21], we can significantly reduce this number from 2500 to 16 and get a fair estimation of the $50 \times 50$ pixel distribution map, shown in Fig. 5(b). Based on this method, to improve the robustness of the control field, we further make an optimization using the BPM method [21] with the objective function defined as the average fidelity

$$\mathcal{F}_{\text{obj}} = \mathcal{N} \sum_{k=1}^{M} \sum_{j=1}^{N} p(\delta_k) p(\kappa_j) f(\delta_k, \kappa_j), \tag{16}$$

where $f(\delta_k, \kappa_j)$ is the fidelity with control field detuning $\delta_k$ and amplitude bias $\kappa_k$ (see Appendix D for details), $p(\delta)$ and $p(\kappa)$ are the normal distributions of $\delta$ and $\kappa$,

$$\begin{aligned} p(\delta) &= \frac{1}{\sqrt{2\pi}\sigma_\delta} e^{-\delta^2/2\sigma_\delta^2} \\ p(\kappa) &= \frac{1}{\sqrt{2\pi}\sigma_\kappa} e^{-\kappa^2/2\sigma_\kappa^2}, \end{aligned} \tag{17}$$

and $\mathcal{N} = [\sum_{k=1}^{M} \sum_{j=1}^{N} p(\delta_k) p(\kappa_j)]^{-1}$ is the normalization constant. The optimization results are presented in Fig. 5(c) and the estimation of Fig. 5(c) using 16 samples is given in Fig. 5(d), which are visibly identical.

## V. CONCLUSION

We have presented a comprehensive comparison of three widely used methods, namely, the GRAPE method, the CRAB method, and the PM method, based on the optimization fidelity, speed, and experimental feasibility. Synthetically, we found that the GRAPE method performs well with high fidelity and rapid optimization speed in a shorter evolution time range, while the PM method shows stable performance for all evolution times within the scope of consideration and is easy to use as it can be accomplished by a direct searching method. In addition, we achieved a fast and accurate estimation as well as optimization of the field robustness using the BPM method. These results provide reference for existing STIRAP shortcut methods in the presence of dissipation [25,26] as well as robust control methods of the NV center [27,28] to further explore and complete each other.

Further optimizations can be carried out based on these methods, including optimization of the magnetic-field amplitudes during the preparation and manipulation process of the system, since the bias of the magnetic field is the common interference factor in typical experiments. One can also apply the methods to closed-loop control that directly uses experimental outputs as the objective function value for

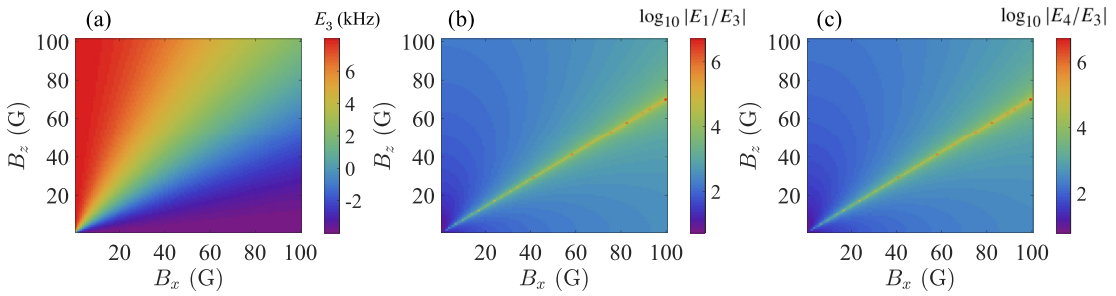


FIG. 6. (a) Explicit value of $E_3$ for different $B_x$ and $B_z$ values. (b) Comparison between $E_1$ and $E_3$, evaluated by $\log_{10}|E_1/E_3|$. (c) Comparison between $E_4$ and $E_3$, evaluated by $\log_{10}|E_4/E_3|$.

exploring a more practical control field during the experimental process [29–31]. More advance investigations and analyses on how the control apparatuses implement the numerical optimized pulses, such as frequency response analysis, will significantly improve the experimental performance of the optimized pulses [32]. The system under consideration could be expanded to scalable multiqubit registers in NV centers [33,34]. Furthermore, our work can straightforwardly be adapted to an alternative system involving an intrinsic nitrogen nuclear spin [35]. Overall, we provided a versatile optimization strategy for improving the performance of a quantum register based on DFS nuclear spin systems in diamond for future quantum computing and sensing technologies.

## ACKNOWLEDGMENTS

J.T. acknowledges support from Natural Science Foundation for Young Scientists of Shanxi Province (Grant No. 202203021222113) and National Natural Science Foundation of China (Grant No. 62305241) and thanks Jianming Cai, Kangze Li, Yaoxing Bian, Jiamin Li, and Shuangping Han for discussions. L.X. and J.T. acknowledge National Natural Science Foundation of China (Grant No. U23A20380) for support. F.J. and R.S.S. acknowledge DFG, BMBF (CoGeQ, SPINNING, QRX), QC-4-BW, Center for Integrated Quantum Science and Technology, and the ERC Synergy Grant HyperQ for support. R.S.S. thanks Philipp Vetter (Ulm), Matthias Müller (FZ Jülich), and Phila Rembold (TU Wien) for discussions. All of the authors are grateful to Jingfu Zhang (Ulm) for his advice and Timo Joas (Ulm) for providing codes in the pulse measurement process.

## APPENDIX A: STATIC HAMILTONIAN

The system under consideration is a tripartite system comprising one $NV^-$ electron spin ($S = 1$) and two proximal $^{13}C$ nuclear spins ($I = 1/2$) [15]. The total time-independent Hamiltonian is [15]

$$H = D\hat{S}_z^2 + \gamma_e \mathbf{B}\cdot\mathbf{S} + \mathbf{S}\cdot\sum_{i=1}^{2}\mathbb{A}^{(i)}\cdot\mathbf{I}^{(i)} + \gamma_c\mathbf{B}\cdot\sum_{i=1}^{2}\mathbf{I}^{(i)} + H_{nn}, \tag{A1}$$

where $D\hat{S}_z^2$ is the zero-field term of the electron spin, $\gamma_e\mathbf{B}\cdot\mathbf{S}$ is the magnetic interaction of the electron spin, $\mathbf{S}\cdot\sum_{i=1}^{2}\mathbb{A}^{(i)}\cdot\mathbf{I}^{(i)}$ is the hyperfine coupling of the electron spin and the nuclear spins, and the hyperfine coupling tensor $\mathbb{A}^{(i)}$ for the $i$th nuclear spin has the form

$$A_{kl}^{(i)} = A_c^{(i)}\delta_{kl} + A_d^{(i)}\left(\delta_{kl} - 3\hat{r}_k^{(i)}\hat{r}_l^{(i)}\right), \tag{A2}$$

with the Fermi constant term $A_c$, the dipolar interaction $A_d$, and $k, l = x, y, z$. The term $\gamma_c\mathbf{B}\cdot\sum_{i=1}^{2}\mathbf{I}^{(i)}$ represents the magnetic interaction of the nuclear spin. The last term follows

$$H_{nn} = \sum_{i<j}\frac{\mu_0\gamma_c^2}{4\pi r_{ij}^3}\left(\mathbf{I}_i\cdot\mathbf{I}_j - \frac{3(\mathbf{I}_i\cdot\mathbf{r}_{ij})(\mathbf{r}_{ij}\cdot\mathbf{I}_j)}{r_{ij}^2}\right). \tag{A3}$$

To achieve the Hamiltonian of Eq. (2), several approximations need to be made. First, negligible quantities can be omitted, including (i) the nonaxial components $S_x$ and $S_y$, which are neglected due to $D \gg \gamma_e B_x$ and $D \gg A_{ij}$, and (ii) the isotropic hyperfine couplings, which are much stronger than the dipolar coupling ($d_{12} = 4$ kHz) and the magnetic interaction terms $\gamma_c Bx$ and $\gamma_c Bz$ (therefore the latter three terms vanish in the $m_s = 1$ Hamiltonian). In addition, we consider a simplified spatial arrangement, where the direction vector $\mathbf{r}$ between the two nuclear spins is assumed to be parallel to the quantization axis $\hat{z}$ and the magnetic field comprises only the $z$ and $x$ directions such that $\mathbf{B} = B_z\hat{z} + B_x\hat{x}$. Further, for a more concise form of the Hamiltonian as well as the system description, the anisotropic hyperfine coupling $A_{\text{ani}}$ is neglected. However, using the full Hamiltonian does not change the main conclusions of the strategy based on the decoherence-free subspace [15].

The explicit formation of eigenstates of the final Hamiltonian of Eq. (2) is shown in Fig. 1(b). Figure 6 gives the explicate value of $E_3$, as well as comparisons between $E_{1\,(4)}$ and $E_3$ when the values of $B_x$ and $B_z$ vary from 1 G to 100 G, indicating that in this range $E_3$ is indeed close to zero compared to $E_1$ and $E_4$.

## APPENDIX B: INITIALIZATION PROCESS

The strategy adopted to access the decoherence-protected subspace is by polarizing the spin system to the state $|0_L\rangle$, which consists of three steps [15]. The first step is to polarize the system to the state $|0\uparrow\uparrow\rangle$, via the application of the magnetic field having the components $B_z \approx 5$ G and $B_x \approx 70$ G. With this magnetic field, the eigenstate $|\psi_1\rangle$ is closely projected to the state $|0\uparrow\uparrow\rangle$. Hence, the system is now approximately polarized to the state $|\psi_1\rangle$. The second step is successively tuning $B_x$ and $B_z$, during which the state $|\psi_1\rangle$

evolves adiabatically to a state that has a balanced contribution of all bare states, reached when the magnetic field arrives at $B_x = 100$ G and $B_z = 5$ G. The last step is the transformation from the state $|\psi_1\rangle$ to $|\psi_2\rangle$, by applying microwave (MW) fields that drive the transitions $|\psi_1\rangle \rightarrow |\psi_6\rangle \rightarrow |\psi_2\rangle$.

## APPENDIX C: DRIVING HAMILTONIAN

In the following, we elaborate the derivation of the driving Hamiltonian [15] to the total system Hamiltonian

$$H = \sum_i E_i \hat{\sigma}_{ii}, \tag{C1}$$

where $\hat{\sigma}_{ij} = |\psi_i\rangle\langle\psi_j|$, with $|\psi_i\rangle$ the eigenstates ($i = 1, \ldots, 8$), and $E_i$ represents the corresponding eigenvalues. Our static system is driven by two MW fields, indexed by $p$ and $s$, giving the driving Hamiltonian as

$$H_{\rm d} = [\sqrt{2}\Omega_p \cos(\omega_p t) + \sqrt{2}\Omega_s \cos(\omega_s t)]\hat{S}_x, \tag{C2}$$

with $\Omega_{p\,(s)}$ and $\omega_{p\,(s)}$ the amplitudes and the frequencies of the two MW fields, respectively, and $\hat{S}_x = (|1\rangle\langle 0| + |0\rangle\langle 1|)/\sqrt{2}$ the $2 \times 2$ subspace of $S = 1$ spin matrices. The interaction Hamiltonian can be written as

$$H^I = (H - H_0) + e^{iH_0 t} H_{\rm d} e^{-iH_0 t}. \tag{C3}$$

To get a more concise expression, we take

$$H_0 = E_1\sigma_{11} + E_2\sigma_{22} + E_6 \sum_{i=5}^{8} \sigma_{ii}; \tag{C4}$$

thus the second term in Eq. (C3) becomes

$$e^{iH_0 t} H_{\rm d} e^{-iH_0 t} = \left( e^{-i\omega_p t} \sum_{i=5}^{8} \chi_{1i}\sigma_{1i} + e^{-i\omega_s t} \sum_{i=6,7} \chi_{2i}\sigma_{2i} + \text{H.c.} \right) \times [\Omega_p \cos(\omega_p t) + \Omega_s \cos(\omega_s t)], \tag{C5}$$

where $\chi_{ij} = \langle\psi_i|\hat{V}|\psi_j\rangle$ and $\hat{V} = \sqrt{2}\hat{S}_x$. Note here that $\chi_{25} = \chi_{52} = \chi_{28} = \chi_{82} = 0$, so they are not shown in Eq. (C5). After using the rotating-wave approximation by removing the rapid oscillation terms with frequencies of $2\omega_{p\,(s)}$ and $\omega_{p\,(s)} \pm \omega_{s\,(p)}$, we finally get the final interaction Hamiltonian

$$H^I_{\rm RWA} = \frac{\Omega_p(t)}{2}(\chi_{51}\hat{\sigma}_{51} + \chi_{61}\hat{\sigma}_{61} + \chi_{71}\hat{\sigma}_{71} + \chi_{81}\hat{\sigma}_{81} + \text{H.c.}) + \frac{\Omega_s(t)}{2}(\chi_{62}\hat{\sigma}_{62} + \chi_{72}\hat{\sigma}_{72} + \text{H.c.}) + (H - H_0). \tag{C6}$$

## APPENDIX D: HAMILTONIAN WITH FIELD DETUNING AND AMPLITUDE BIAS

When considering the frequency detuning $\delta$ and amplitude bias $\kappa$ of the control fields, the driving Hamiltonian can be represented as

$$H_{\rm d} = \sqrt{2}(1+\kappa)[\Omega_p \cos(\omega'_p t) + \Omega_s \cos(\omega'_s t)]\hat{S}_x, \tag{D1}$$

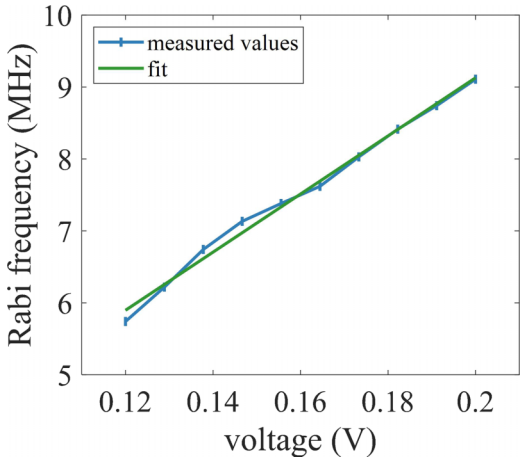


FIG. 7. Calibration curve between the input voltage from the AWG and the measured Rabi frequency from a single NV experiment. The fit values are $a_\Omega = 40.4 \pm 1.2$ MHz/V and $b_\Omega = 1.0 \pm 0.2$ V.

where $\omega'_p = E_6 - E_1 + \delta$ and $\omega'_s = E_6 - E_2 + \delta$. Taking $H_0$ as

$$H_0 = E_1\sigma_{11} + E_2\sigma_{22} + (E_6 + \delta)\sum_{i=5}^{8} \sigma_{ii}, \tag{D2}$$

we have

$$e^{iH_0 t} H_{\rm d} e^{-iH_0 t} = \left( e^{-i\omega'_p t} \sum_{i=5}^{8} \chi_{1i}\sigma_{1i} + e^{-i\omega'_s t} \sum_{i=6,7} \chi_{2i}\sigma_{2i} + \text{H.c.} \right) \times [(1+\kappa)\Omega_p \cos(\omega'_p t) + (1+\kappa)\Omega_s \cos(\omega'_s t)]. \tag{D3}$$

Again, we neglect the rapid oscillation terms with frequencies of $2\omega'_{p\,(s)}$ and $\omega'_{p\,(s)} \pm \omega'_{s\,(p)}$, and the interaction Hamiltonian

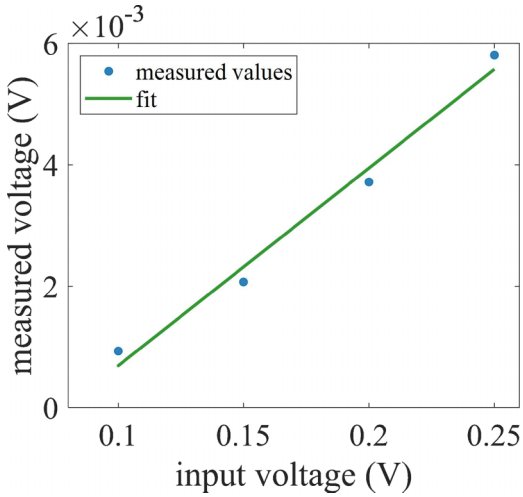


FIG. 8. Calibration curve between the input voltage from the AWG and the measured voltage from the oscilloscope. The fit values are $a_{\text{osc-AWG}} = 0.016 \pm 0.003$ $\text{V}_{\text{osci}}/\text{V}_{\text{AWG}}$ and $b_{\text{osc-AWG}} = -0.0026 \pm 0.0006$ $\text{V}_{\text{osci}}$.

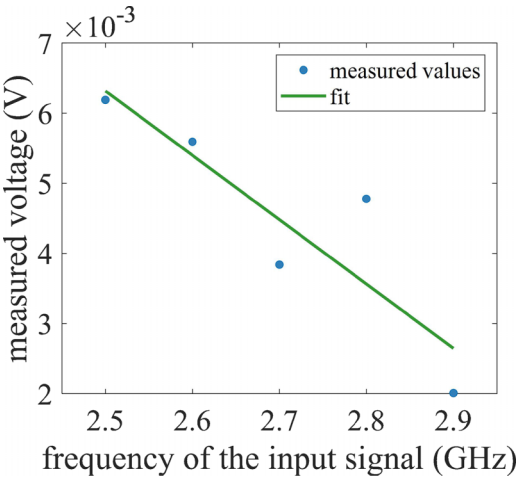


FIG. 9. Calibration curve for the relation between the frequency of the input signal and the measured voltage from the oscilloscope (with an input voltage of 230 mV). The parameters are $a_{V-f} = -0.0092 \pm 0.0028$ V/GHz and $b_{V-f} = 0.029 \pm 0.008$ V.

becomes

$$H^I_{\mathrm{RWA}} = \frac{(1+\kappa)\Omega_p(t)}{2}(\chi_{51}\hat{\sigma}_{51} + \chi_{61}\hat{\sigma}_{61} + \chi_{71}\hat{\sigma}_{71} + \chi_{81}\hat{\sigma}_{81} + \mathrm{H.c.}) + \frac{(1+\kappa)\Omega_s(t)}{2}(\chi_{62}\hat{\sigma}_{62} + \chi_{72}\hat{\sigma}_{72} + \mathrm{H.c.}) + \sum_{i=3,4} E_i\hat{\sigma}_{ii} + \sum_{i=5}^{8}(E_i - E_6 - \delta)\hat{\sigma}_{ii}. \quad \text{(D4)}$$

Using this Hamiltonian and according to Eq. (8), we can obtain the density matrix $\rho(T, \delta, \kappa)$ at time $T$. Similar to Eq. (9), the fidelity with detuning $\delta$ and amplitude bias $\kappa$ can be represented as

$$f(\delta, \kappa) = \mathrm{Tr}[\langle\psi_2|\rho(T, \delta, \kappa)|\psi_2\rangle] \quad \text{(D5)}$$

and the average fidelity for different $\delta$ and $\kappa$ can be calculated by Eq. (16).

## APPENDIX E: PULSE CALIBRATION

The method given in this paper for experimentally determining the Rabi frequencies for different pulse shapes is performed by using a linear relationship between the Rabi frequencies and the MW amplitudes from an AWG [24]. This relationship holds due to the small ratio between the transition frequency in the gigahertz range (2.9 GHz) and the Rabi frequency in the range of several tens of megahertz. Through the pulse calibrations in the experiment, we use our built-in signal processing and analysis software Qudi [36].

For further translation of the pulsed signal from the oscilloscope voltage signal to the Rabi frequency (see Fig. 7), the same linear matching procedure is performed between the voltage from the AWG and the amplified signal

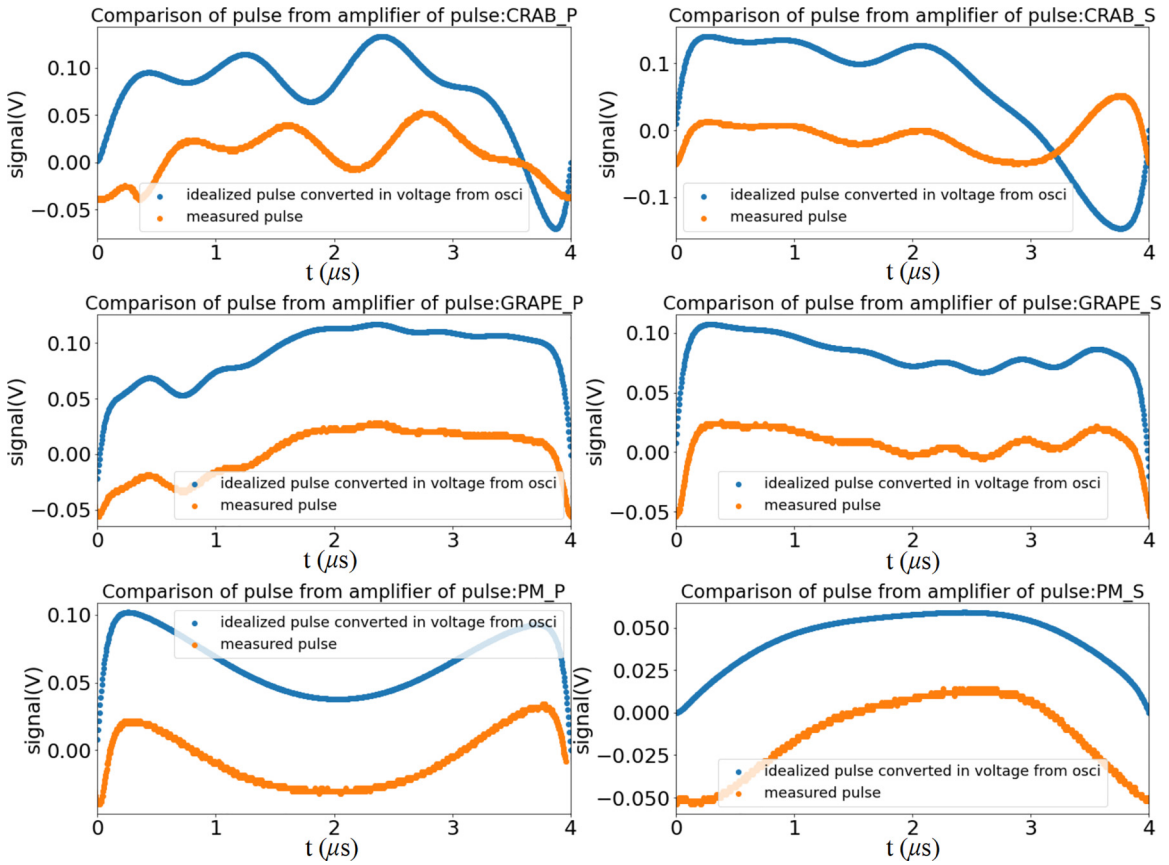


FIG. 10. Comparison of the pulse shapes. For clarity, the scale is predetermined to simply compare the pulse shapes from the numerically obtained pulses and the measured ones. For the case of $\Omega_s$ obtained via the CRAB method at time of 3 μs, the amplitude goes up according to the pulse envelope of the electronic signal.

amplitude measured by the oscilloscope (see Fig. 8). Also, we perform an analysis of the relationship between the signal at constant AWG voltage and different frequencies of the MW signals. This is due to fact that the oscilloscope has a certain bandwidth where the amplitude varies at different frequencies (here the oscilloscope used has an operating bandwidth up to 300 MHz). After the critical value it has a certain damping, which has a linear behavior at the higher-frequency range (see Fig. 9).

Here the relation between the measured voltage of the oscilloscope $V_{\text{osci}}$ and the voltage inserted in the AWG $V_{\text{AWG}}$ is obtained by the linear equation $V_{\text{osci}} = aV_{\text{AWG}} + b$, with the scaling factor $a$ and an offset $b$, obtained by linear regression. We use the same procedure to establish the relations among the Rabi frequency $\Omega$, the voltage $V_{\text{AWG}}$, and the signal frequency $f$. From these previous measurements the comparison between the experimental data and the simulated data is done (see Fig. 10).


[1] N. Aslam, M. Pfender, P. Neumann, R. Reuter, A. Zappe, F. Fávaro De Oliveira, A. Denisenko, H. Sumiya, S. Onoda, J. Isoya, and J. Wrachtrup, Nanoscale nuclear magnetic resonance with chemical resolution, Science **357**, 67 (2017).

[2] S. Zaiser, T. Rendler, I. Jakobi, T. Wolf, S.-Y. Lee, S. Wagner, V. Bergholm, T. Schulte-Herbrüggen, P. Neumann, and J. Wrachtrup, Enhancing quantum sensing sensitivity by a quantum memory, Nat. Commun. **7**, 12279 (2016).

[3] J. Zhou, W.-C. Yu, Y.-M. Gao, and Z.-Y. Xue, Cavity QED implementation of non-adiabatic holonomies for universal quantum gates in decoherence-free subspaces with nitrogen-vacancy centers, Opt. Express **23**, 14027 (2015).

[4] M.-R. Yun, F.-Q. Guo, L.-L. Yan, E. Liang, Y. Zhang, S.-L. Su, C. X. Shan, and Y. Jia, Parallel-path implementation of nonadiabatic geometric quantum gates in a decoherence-free subspace with nitrogen-vacancy centers, Phys. Rev. A **105**, 012611 (2022).

[5] K. R. K. Rao and D. Suter, Level anti-crossings of a nitrogen-vacancy center in diamond: Decoherence-free subspaces and 3D sensors of microwave magnetic fields, New J. Phys. **22**, 103065 (2020).

[6] P. G. Kwiat, A. J. Berglund, J. B. Altepeter, and A. G. White, Experimental verification of decoherence-free subspaces, Science **290**, 498 (2000).

[7] L.-A. Wu and D. A. Lidar, Creating decoherence-free subspaces using strong and fast pulses, Phys. Rev. Lett. **88**, 207902 (2002).

[8] A. F. Kockum, G. Johansson, and F. Nori, Decoherence-free interaction between giant atoms in waveguide quantum electrodynamics, Phys. Rev. Lett. **120**, 140404 (2018).

[9] D. Kielpinski, V. Meyer, M. A. Rowe, C. A. Sackett, W. M. Itano, C. Monroe, and D. J. Wineland, A decoherence-free quantum memory using trapped ions, Science **291**, 1013 (2001).

[10] L.-A. Wu, P. Zanardi, and D. A. Lidar, Holonomic quantum computation in decoherence-free subspaces, Phys. Rev. Lett. **95**, 130501 (2005).

[11] J. M. Taylor, W. Dür, P. Zoller, A. Yacoby, C. M. Marcus, and M. D. Lukin, Solid-state circuit for spin entanglement generation and purification, Phys. Rev. Lett. **94**, 236803 (2005).

[12] J. T. Reilly, S. B. Jäger, J. Cooper, and M. J. Holland, Adiabatic control of decoherence-free subspaces in an open collective system, Phys. Rev. A **106**, 023703 (2022).

[13] W. Su, W. Qin, A. Miranowicz, T. Li, and F. Nori, Heralded quantum entangling gate for distributed quantum computation in a decoherence-free subspace, arXiv:2305.00642.

[14] X. Hu, F. Zhang, Y. Li, and G. Long, Optimizing quantum gates within decoherence-free subspaces, Phys. Rev. A **104**, 062612 (2021).

[15] F. J. González and R. Coto, Decoherence-protected quantum register of nuclear spins in diamond, Quantum Sci. Technol. **7**, 025015 (2022).

[16] X. Chen, I. Lizuain, A. Ruschhaupt, D. Guéry-Odelin, and J. G. Muga, Shortcut to adiabatic passage in two- and three-level atoms, Phys. Rev. Lett. **105**, 123003 (2010).

[17] S. Sangtawesin, C. A. McLellan, B. A. Myers, A. C. B. Jayich, D. D. Awschalom, and J. R. Petta, Hyperfine-enhanced gyromagnetic ratio of a nuclear spin in diamond, New J. Phys. **18**, 083016 (2016).

[18] N. Khaneja, T. Reiss, C. Kehlet, T. Schulte-Herbrüggen, and S. J. Glaser, Optimal control of coupled spin dynamics: Design of NMR pulse sequences by gradient ascent algorithms, J. Magn. Reson. **172**, 296 (2005).

[19] T. Caneva, T. Calarco, and S. Montangero, Chopped random-basis quantum optimization, Phys. Rev. A **84**, 022326 (2011).

[20] J. Tian, H. Liu, Y. Liu, P. Yang, R. Betzholz, R. S. Said, F. Jelezko, and J. Cai, Quantum optimal control using phase-modulated driving fields, Phys. Rev. A **102**, 043707 (2020).

[21] J. Tian, R. S. Said, F. Jelezko, J. Cai, and L. Xiao, Bayesian-based hybrid method for rapid optimization of NV center sensors, Sensors **23**, 3244 (2023).

[22] R. Hanson, F. M. Mendoza, R. J. Epstein, and D. D. Awschalom, Polarization and readout of coupled single spins in diamond, Phys. Rev. Lett. **97**, 087601 (2006).

[23] S. S. Hegde, J. Zhang, and D. Suter, Efficient quantum gates for individual nuclear spin qubits by indirect control, Phys. Rev. Lett. **124**, 220501 (2020).

[24] J. Scheuer, X. Kong, R. S. Said, J. Chen, A. Kurz, L. Marseglia, J. Du, P. R. Hemmer, S. Montangero, T. Calarco, B. Naydenov, and F. Jelezko, Precise qubit control beyond the rotating wave approximation, New J. Phys. **16**, 093022 (2014).

[25] D. Stefanatos and E. Paspalakis, Optimal shortcuts of stimulated Raman adiabatic passage in the presence of dissipation, Philos. Trans. R. Soc. A **380**, 20210283 (2022).

[26] V. Evangelakos, E. Paspalakis, and D. Stefanatos, Optimal STIRAP shortcuts using the spin-to-spring mapping, Phys. Rev. A **107**, 052606 (2023).

[27] N. Oshnik, P. Rembold, T. Calarco, S. Montangero, E. Neu, and M. M. Müller, Robust magnetometry with single nitrogen-vacancy centers via two-step optimization, Phys. Rev. A **106**, 013107 (2022).

[28] A. F. L. Poulsen, J. D. Clement, J. L. Webb, R. H. Jensen, L. Troise, K. Berg-Sørensen, A. Huck, and U. L. Andersen, Optimal control of a nitrogen-vacancy spin ensemble in diamond for sensing in the pulsed domain, Phys. Rev. B **106**, 014202 (2022).

[29] G. Feng, F. H. Cho, H. Katiyar, J. Li, D. Lu, J. Baugh, and R. Laflamme, Gradient-based closed-loop quantum optimal control in a solid-state two-qubit system, Phys. Rev. A **98**, 052341 (2018).

[30] C. Chen, L.-C. Wang, and Y. Wang, Closed-loop and robust control of quantum systems, Sci. World J. **2013**, e869285 (2013).

[31] C. P. Koch, U. Boscain, T. Calarco, G. Dirr, S. Filipp, S. J. Glaser, R. Kosloff, S. Montangero, T. Schulte-Herbrüggen, D. Sugny, and F. K. Wilhelm, Quantum optimal control in quantum technologies. Strategic report on current status, visions and goals for research in Europe, EPJ Quantum Technol. **9**, 19 (2022).

[32] J. Singh, R. Zeier, T. Calarco, and F. Motzoi, Compensating for nonlinear distortions in controlled quantum systems, Phys. Rev. Appl. **19**, 064067 (2023).

[33] C. E. Bradley, J. Randall, M. H. Abobeih, R. C. Berrevoets, M. J. Degen, M. A. Bakker, M. Markham, D. J. Twitchen, and T. H. Taminiau, A ten-qubit solid-state spin register with quantum memory up to one minute, Phys. Rev. X **9**, 031045 (2019).

[34] D. Maile and J. Ankerhold, Performance of quantum registers in diamond in the presence of spin impurities, arXiv:2211.06234.

[35] J. Zhang, S. S. Hegde, and D. Suter, Efficient implementation of a quantum algorithm in a single nitrogen-vacancy center of diamond, Phys. Rev. Lett. **125**, 030501 (2020).

[36] J. M. Binder, A. Stark, N. Tomek, J. Scheuer, F. Frank, K. D. Jahnke, C. Müller, S. Schmitt, M. H. Metsch, T. Unden, T. Gehring, A. Huck, U. L. Andersen, L. J. Rogers, and F. Jelezko, Qudi: A modular python suite for experiment control and data processing, SoftwareX **6**, 85 (2017).